Real-Time Observation of AZ91 Solidification by Synchrotron Radiography

G. Zeng, K. Nogita, S. Belyakov, J.W. Xian, S.D. McDonald, K.V. Yang, H. Yasuda, and C.M. Gourlay

Abstract

The equiaxed solidification of AZ91 has been studied by time-resolved synchrotron radiography of 150 μm thick samples. Primary Al_8Mn_5 and α-Mg dendrite growth has been observed and analysed during solidification at a cooling rate of 5 K/min. Morphological, compositional and kinetic information of AZ91 solidification has been extracted from quantitative image analysis on synchrotron radiographs combined with thermodynamic calculations. α-Mg dendrites appeared to grow largely independently of the surrounding Al_8Mn_5 particles. Solute partitioning mainly occurred during the dendrite coarsening stage and Zn/Al solute build-up was studied in a region that remains a liquid channel until a late stage of AZ91 solidification.

Keywords

AZ91 alloy • Synchrotron imaging • Solidification

Introduction

AZ series (Mg–Al–Zn–Mn) alloys, especially AZ91, are often used in the automotive industry due to their low density, high specific strength at room temperature, castability, machinability etc. [1]. Mn additions to Mg–Al–Zn alloys result in the formation of Al–Mn–Fe-based intermetallics from the melt [2] which significantly improves the corrosion resistance [3]. On the other hand, the small amount of Mn significantly alters the solidification path of Mg–Al–Zn alloys [4]. AZ91 alloys exhibit non-equilibrium solidification at cooling rates as low as 1 K/min [5] which means that $Mg_{17}Al_{12}$ forms under all industrial cooling conditions and the Al–Mn intermetallics that form can vary with cooling rate. Previous studies have been performed to understand growth morphologies and orientations of α-Mg and also intermetallics in AZ91 [6–11]. In this work, we aim to build further understanding of the development of microstructure in AZ91 using in situ synchrotron radiography during equiaxed solidification.

Conventionally we characterise fully solidified microstructures after the specimen has cooled to room temperature, or observe the quenched or decanted microstructure by interrupting solidification at a certain temperature in the mushy zone. It is difficult to fully understand solidification behaviour of multicomponent alloys by these methods in the cases where many phases are involved. For instance, Al and Mn alloying and Fe pick-up in AZ series alloys result in the formation of various types of intermetallics [12–15], that form throughout the different stages of solidification. Under certain circumstances one phase, such as Al_8Mn_5, is involved in multiple reactions

G. Zeng (✉) · S. Belyakov · J.W. Xian · C.M. Gourlay
Department of Materials, Imperial College,
London, SW7 2AZ, UK
e-mail: g.zeng@imperial.ac.uk

K. Nogita · S.D. McDonald
NS CMEM, School of Mechanical and Mining Engineering,
The University of Queensland, St Lucia, QLD 4072, Australia

K.V. Yang
Department of Materials Science and Engineering,
Monash University, Clayton, VIC 3800, Australia

H. Yasuda
Department of Materials Science and Engineering,
Kyoto University, Sakyo-Ku, Kyoto, 606-8501, Japan

over a wide temperature range [5, 16, 17]. These are difficult to be fully resolved by post solidification microstructure characterisation. Therefore, it is highly desirable to directly observe nucleation, growth and the interaction of different phases to more fully understand the whole solidification process. Meanwhile, the CALPHAD approach [18] has been used as a powerful tool for phase diagram and thermodynamic calculation of multicomponent systems such as the Mg–Al–Zn and Mg–Al–Zn–Mn systems [19]. Thermodynamic calculation provides valuable information about the solidification path under both equilibrium and Scheil conditions. These include the reaction temperature range, phase formation/reactions, composition variation etc., which are difficult to be comprehensively understood from only microstructure characterisation.

Over the last decades, the development of X-ray imaging techniques using high brightness synchrotron radiation has enabled the real-time observation of solidification behaviour in metallic systems [20, 21]. This has advanced the understanding of complex crystal growth processes and the evolving solidification microstructure, providing substantial morphological, solutal and kinetic information [22]. Due to the difference of X-ray attenuation of the alloy components and also with the help of phase contrast by coherent X-rays, solid/liquid interfaces during solidification can be observed with sufficient spatial-temporal resolution [23]. It has been successfully used for observing solidification phenomena in various alloys such as Al–Cu [20, 24], Al–Ge [25], Sn–Bi [26], Sn–Cu [27, 28], Fe–C [23, 29] etc. For in situ observation of solidification in magnesium alloys, there are additional challenges due to oxidation and reactivity of the magnesium melt at high temperature compared to the aforementioned systems, and various groups have recently adapted synchrotron imaging to Mg alloys [30, 31]. Now, in situ radiography is a powerful and unique tool for understanding the solidification path and kinetics of multicomponent magnesium alloys, particularly when used in parallel with thermodynamic calculations and thermal analysis.

This paper is a preliminary study of the solidification of AZ91 by synchrotron X-ray radiography combined with thermodynamic calculations. We focus on Al_8Mn_5 and αMg microstructure evolution and solute partitioning during dendrite growth and coarsening.

Procedures

AZ91 alloy was cast, sliced and polished to 0.15 mm thickness for synchrotron radiography experiments. The composition of the specimens was verified by means of inductively coupled plasma mass spectrometry, as shown in Table 1 (all composition are in wt%). This composition (Mg–8.21Al–0.71Zn–0.14Mn) was also used as an input to calculate the solidification path of AZ91 under both equilibrium and Scheil conditions, using the Mg database PanMg8 in PanDat® (Computherm, Madison, WI. USA) software.

Synchrotron radiography experiments were performed on beamline BL20B2 at SPring-8 in Hyogo, Japan. A temperature/atmosphere controlled furnace enabled real-time synchrotron radiography experiments (Fig. 1a) and details are described elsewhere [29]. Experiments were performed under 10^{-1} torr vacuum in the furnace chamber, and the specimen was confined between two MgO plates, preventing oxidation and reaction of the molten magnesium alloy. The configuration of the solidification cell within the furnace is shown in Fig. 1b. Radiography experiments were performed with a monochromatic X-ray with 13 keV photon energy. Specimens with dimensions of 7 mm × 7 mm × 0.15 mm were placed in the solidification cell. The specimen was melted and subsequently cooled at a constant rate of 5 K/min. During cooling, transmitted X-ray images were recorded at the rate of 1 fps, with a field of view (FoV) of 2048 × 2048 pixels, corresponding to 5.53 mm × 5.53 mm. The imposed thermal gradient caused by the temperature control unit (graphite heater located above the field of view), led to a temperature difference of 2–3 K across the
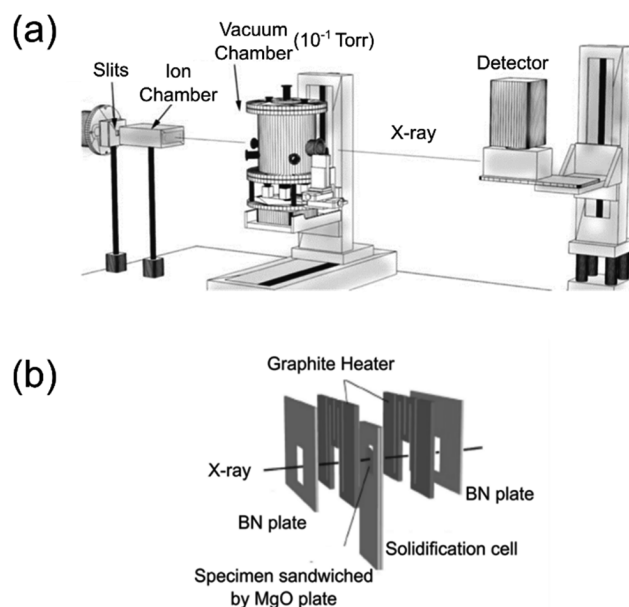
Fig. 1 Experimental setup for the real-time observation of Mg alloy solidification **a** setup at BL20B2 beamline at SPring-8. **b** Solidification cell configuration used for the AZ91 alloy

Table 1 Alloy composition measured by ICP-AES (wt%)

Mg	Al	Zn	Mn	Cu	Si	Ni	Fe	Ca	Be	Cr	Zr
Bal.	8.210	0.710	0.140	0.003	0.020	0.004	<0.001	0.001	<0.001	<0.001	<0.002

FoV (with the top of the sample being hotter than the bottom).

Image processing and analysis were performed using Matlab® and ImageJ. A flat field correction was applied using dark and flat field images which were recorded separately during the experiments. Frame averaging every 10 frames was applied on the dataset for a better signal to noise (S/N) ratio. Enhanced contrast and time averaged image sequences were used for quantification of microstructure evolution with time during solidification of AZ91. Global thresholding of solid/liquid phases was performed using the Otsu method [32].

Results and Discussion

The predicted solidification path calculated for both equilibrium and Scheil conditions in PanDat® is shown in Fig. 2a, b is a magnified version of the earliest stages of solidification. It can be seen that Al_8Mn_5 is the predicted primary phase which forms first from the liquid for both the equilibrium and Scheil approximations. After growth of primary Al_8Mn_5, α-Mg grows with Al_8Mn_5 in the form of L → Al_8Mn_5 + α-Mg. On further cooling, α-Mg continues to grow with other Al_xMn_y intermetallics. For Scheil conditions (i.e. no solid diffusion), solidification ends with a ternary eutectic reaction involving $Mg_{17}Al_{12}$. No $Mg_{17}Al_{12}$ forms in equilibrium solidification. Figure 3 shows radiographs of the evolving microstructure of AZ91 solidifying in

the early stages of solidification at a cooling rate of 5 K/min. The images display the intensity of each pixel using a full range colour map. At the beginning, the FoV of the specimen is mostly liquid with a small fraction of unmelted Al_8Mn_5 particles (dark phases in the image sequence). α-Mg dendrites, which appear as the phase with higher intensity, gradually grew across the FoV. In the reaction of L → Al_8Mn_5 + α-Mg, α-Mg dendrites grew largely independently in the form of equiaxed dendrites, with limited interaction with the Al_8Mn_5 in the 2D projected radiographs.
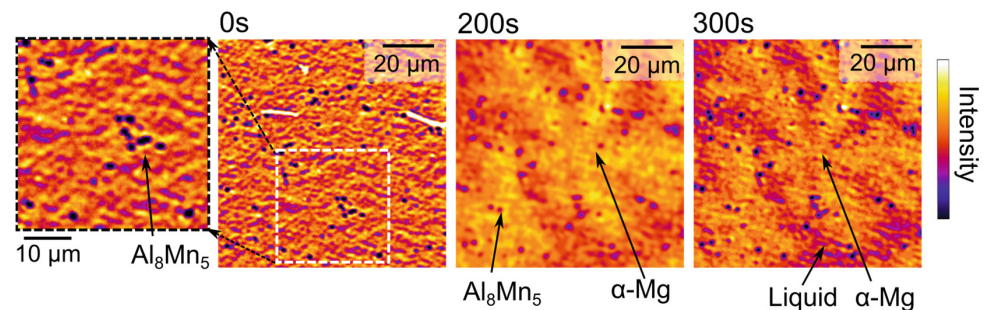
Figure 4 shows microstructure evolution during AZ91 solidification spanning 1108 s. Note that the magnification is lower in Fig. 4 than in Fig. 3. As the temperature decreased and the solid fraction increased, the contrast between the liquid and surrounding dendrites gradually increased due to solute rejection at dendrite growth fronts and the resulting change in X-ray attenuation (i.e. reduction in X-ray intensity) as described in the following analysis.

Solute partitioning to the liquid phase during solidification can be analysed by combining thermodynamic and attenuation calculations. Figure 5a is a plot of the concentration of Mg, Al, Zn and Mn in the liquid as a function of solid fraction assuming Scheil solidification of Mg–8.21Al–0.71Zn–0.14Mn in PanDat. Note that data are plotted only up to ∼85% solid so as to exclude the liquid composition once the $Mg_{17}Al_{12}$ phase forms. The accumulation of Al and Zn solute in the liquid due to partitioning is clear. The mass attenuation coefficient $\frac{\mu}{\rho}$ of the liquid can be calculated from a mass additivity on the liquid composition (Eq. 1). Note

Fig. 2 Solidification path of AZ91 calculated from Pandat® with the PanMg8 database **a** full solidification range **b** initial reactions in the early stages of AZ91 solidification
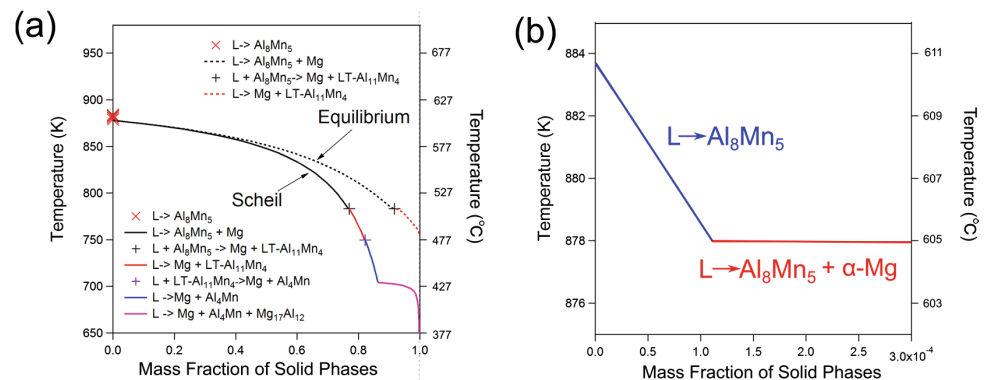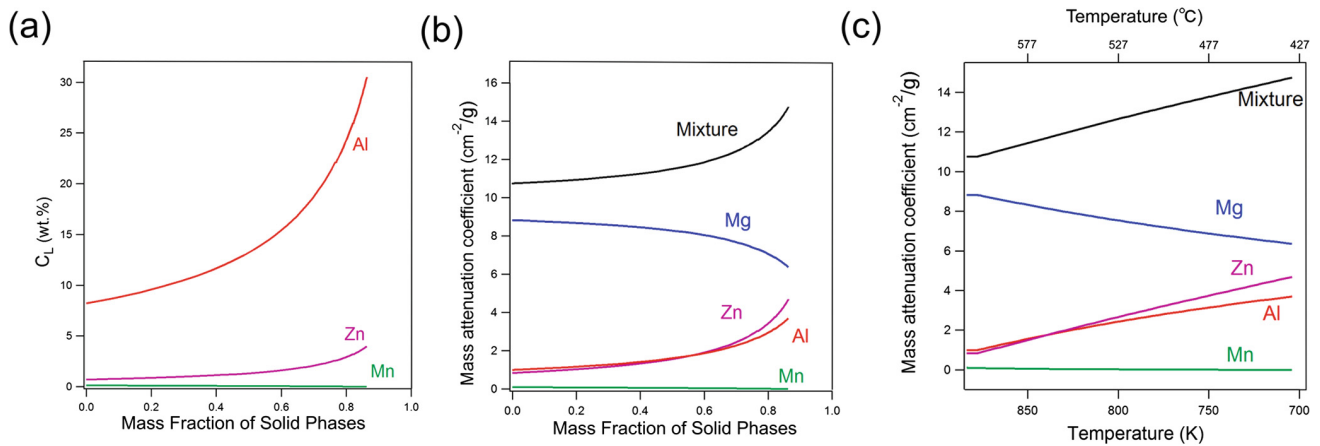

Fig. 3 Al_8Mn_5 formation from the liquid prior to α-Mg dendrite nucleation at 5 K/min
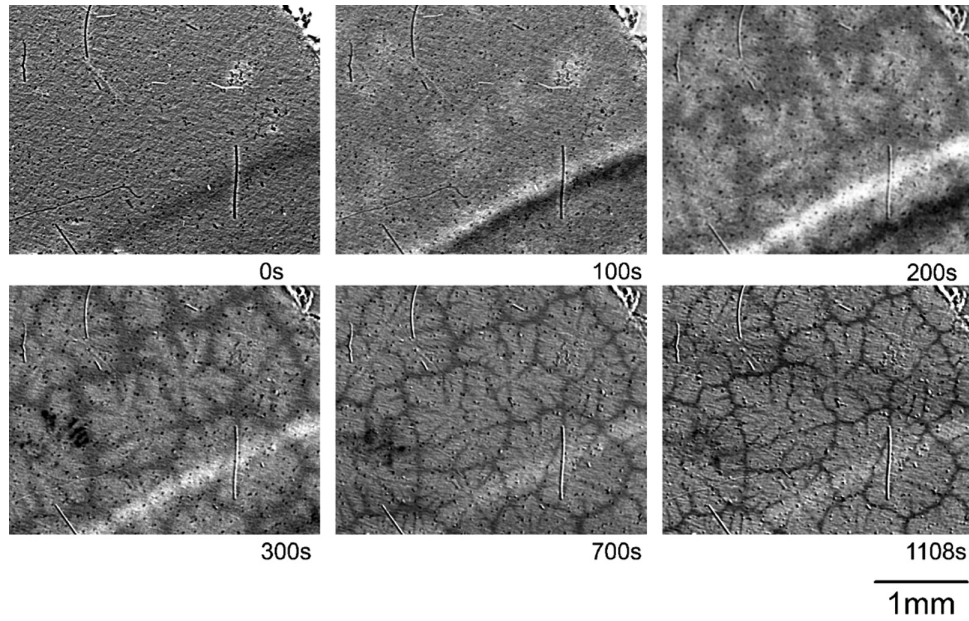
Fig. 4 Radiographs of microstructure evolution in AZ91 solidifying at a cooling rate of 5 K/min

Fig. 5 a Variation in liquid composition during Scheil solidification, calculated from PanDat® with PanMg8. Mg content is 100–(Al + Zn + Mn). **b–c** Mass attenuation coefficient (at 13 keV) of the liquid and the contributions of Mg, Al, Zn and Mn: (**b**) as a function of mass fraction of solid, (**c**) as a function of temperature

that the contribution to attenuation from the minority elements Cu, Ni, Si etc. in AZ91 are negligible, so the mass attenuation coefficient of the liquid can be expressed as Eq. 2.

$$\left(\frac{\mu}{\rho}\right) = \sum_i w_i \left(\frac{\mu}{\rho}\right)_i \qquad (1)$$

$$\left(\frac{\mu}{\rho}\right)_L = w_{Mg}\cdot\left(\frac{\mu}{\rho}\right)_{Mg} + w_{Al}\cdot\left(\frac{\mu}{\rho}\right)_{Al} + w_{Zn}\cdot\left(\frac{\mu}{\rho}\right)_{Zn} + w_{Mn}\cdot\left(\frac{\mu}{\rho}\right)_{Mn} \qquad (2)$$

The linear attenuation coefficient μ_L, then depends on the density of the liquid ρ.

$$\mu_L = \rho\left(\frac{\mu}{\rho}\right)_L \qquad (3)$$

Figure 5b, c show the variation of mass attenuation coefficient of the liquid and also the partial mass attenuation coefficient of each element in the liquid with increasing solid fraction/decreasing temperature in the mushy zone. They show that both Al and Zn are influential at providing

absorption contrast in the X-ray images; for Al because it is so concentrated in the liquid, while for Zn because it is highly attenuating compared to Mg and Al at 13 keV and is rejected into the liquid until late during solidification. It can also be seen in Fig. 5b that, by ~70% solid, Zn solute contributes more to attenuation that Al solute even though there is ~3.3 times more Al in the liquid (Fig. 5a).

The intensity change in the liquid region is indicative of the changing liquid composition (as predicted in Fig. 5) and density. This can be monitored by determining the ratio of liquid intensity to the initial liquid intensity. The first step was adaptive thresholding of image sequences to generate a binary mask of the solid pixels. Therefore, only liquid pixels were included in this analysis. The second step was to convert the X-ray images to constitutional information. The transmitted intensity I_T is given by the Beer-Lambert law;

$$I_T = I_0 e^{-(\mu_{cell}\delta_{cell})} e^{-(\mu_L . \delta)} \tag{4}$$

Fig. 6 Quantification of solute partitioning in the remaining liquid between α-Mg dendrite arms. Data is averaged along Z and plotted versus X and time
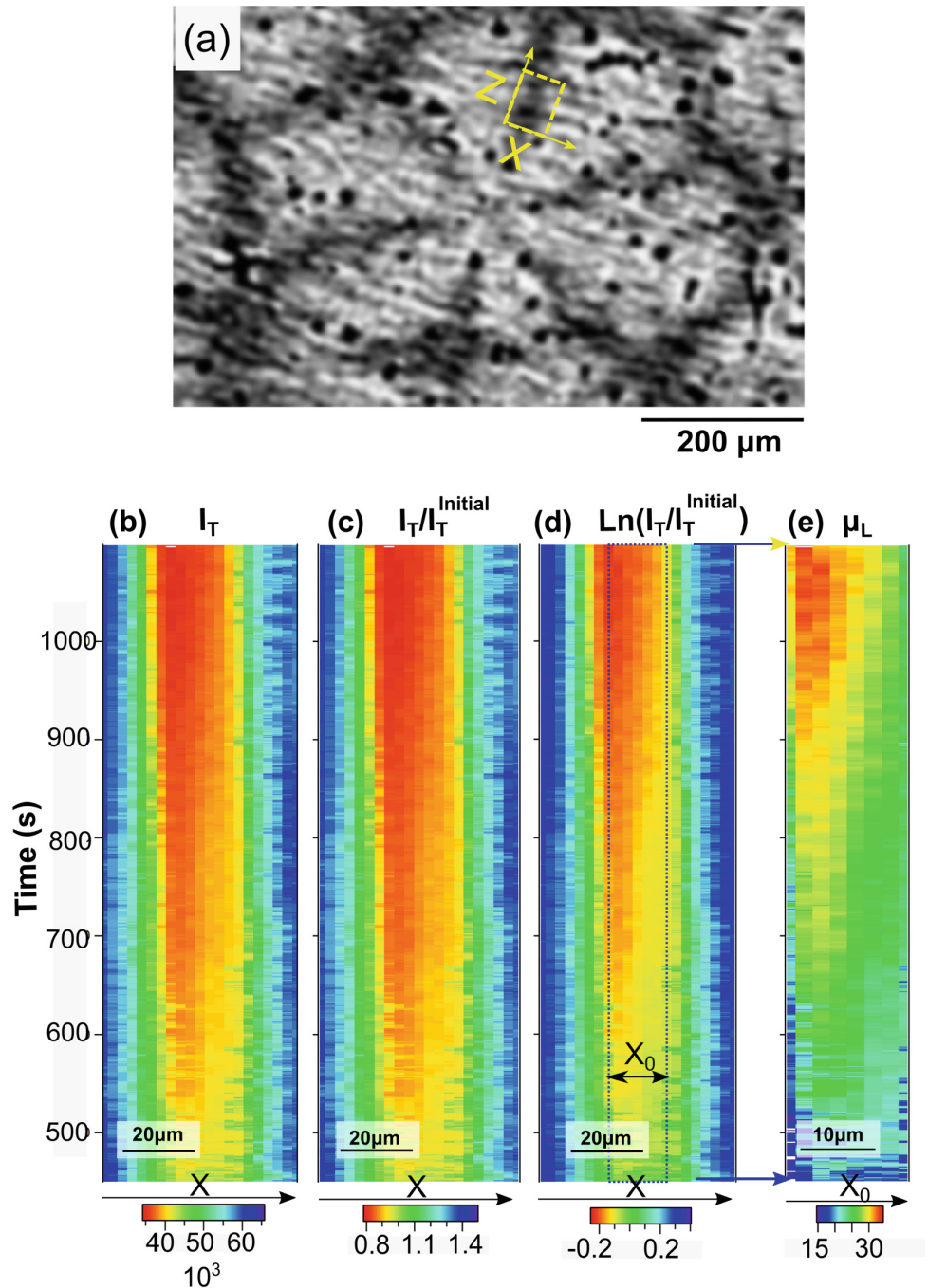
Where I_0 is the incident beam intensity, μ_{cell} and μ_L are the linear attenuation coefficients of the cell and liquid respectively and δ_{cell} and δ are the thickness of the solidification cell and the AZ91 specimen respectively. Taking the ratio of the transmitted intensity through the liquid at a moment during solidification to the transmitted intensity through the liquid at the liquidus temperature, $I_T^{initial}$,

$$\frac{I_T}{I_T^{initial}} = \frac{I_0 e^{-\{(\mu_{cell}\delta) + (\mu_L.\delta)\}}}{I_0 e^{-\{(\mu_{cell}\delta) + (\mu_L^{initial}.\delta)\}}} = e^{\{\mu_L^{initial}.\delta - \mu_L.\delta\}} \quad (5)$$

$$\ln\left(\frac{I_T}{I_T^{initial}}\right) = (\mu_L^{initial} - \mu_L)\delta \quad (6)$$

where the linear attenuation coefficient of the liquid $\mu_L^{initial}$ was obtained from the bulk alloy composition (Mg–8.21Al–0.71Zn–0.14Mn) and the density of liquid AZ91 at the liquidus temperature. Therefore, the mass attenuation coefficient of the local liquid during solidification can be written as follows;

$$\mu_L(C_L, T) = 17.77 - \frac{1}{\delta}\ln\left(\frac{I_T}{I_T^{initial}}\right) \quad (7)$$

To apply the procedure described above, as shown in Fig. 6a, a six-fold α-Mg dendrite was chosen from the image sequence and an inter-dendritic area (the rectangle area in Fig. 6a) between two dendrite arms was studied. Liquid pixels were assigned into bins of constant distance from the α-Mg dendrite arm (binned along the Z direction marked in Fig. 6a). Then the mean intensity of liquid pixels in each bin was found and is plotted in Fig. 6b as function of frame number (time). In Fig. 6c the liquid intensity has been divided by the initial liquid intensity and plotted as a function of position and time. Using Eqs. 5 and 6, $Ln(I_T/I_T^{Initial})$ as a function of position and time are plotted in Fig. 6d. Subsequently μ_L can be obtained as shown in Fig. 6e. These calculations in Figs. 5 and 6 show how solute builds up between the dendrite arms during dendrite coarsening stage. For this multicomponent alloy, the different solutes cannot be separated by this type of analysis but the combined effects of Zn and Al are in reasonable agreement with a solidification path intermediate between the Scheil and equilibrium models.

Conclusions

Microstructure evolution during AZ91 solidification was studied by real-time synchrotron radiography. Quantitative image analysis of the radiograph sequences was combined with thermodynamic calculations to study the formation of Al$_8$Mn$_5$, α-Mg equiaxed dendrite development and solute partitioning at solid-liquid interfaces.

The absorption contrast between the liquid and α-Mg is explored by combining thermodynamic calculations of the liquid composition in PanDat with the attenuation coefficients of the solutes. This showed that Zn is an important solute for absorption contrast and significantly improves the imaging of AZ91 solidification. Solute partitioning mainly occurred during the dendrite coarsening stage and Zn/Al solute build-up was studied in a region that remains a liquid channel until a late stage of AZ91 solidification.

A suitable method to investigate the interactions between primary Al$_8$Mn$_5$ particles and α-Mg dendrites was established. α-Mg dendrites appeared to grow largely independently of the surrounding Al$_8$Mn$_5$ particles.

References

1. B.L. Mordike, T. Ebert, Magnesium properties—applications—potential. Mater. Sci. Eng. A **302**, 37–45 (2001)
2. E.F. Emley, *Principles of Magnesium Technology* (Elsevier Science & Technology, Oxford, 1966), pp. 157–159
3. M. Liu, P.J. Uggowitzer, A.V. Nagasekhar, P. Schmutz, M. Easton, G.L. Song, A. Atrens, Calculated phase diagrams and the corrosion of die-cast Mg-Al alloys. Corros. Sci. **51**, 602–619 (2009)
4. M. Ohno, D. Mirkovic, R. Schmid-Fetzer, Phase equilibria and solidification of Mg-rich Mg-Al-Zn alloys. Mater. Sci. Eng. A **421**, 328–337 (2006)
5. M. Ohno, D. Mirkovic, R. Schmid-Fetzer, Liquidus and solidus temperatures of Mg-rich Mg-Al-Mn-Zn alloys. Acta Mater. **54**, 3883–3891 (2006)
6. S. Biswas, F. Sket, M. Chiumenti, I. Gutiérrez-Urrutia, J.M. Molina-Aldareguía, M.T. Pérez-Prado, Relationship between the 3D porosity and β-phase distributions and the mechanical properties of a high pressure die cast AZ91 Mg alloy. Metall. Mater. Trans. A **44**, 4391–4403 (2013)
7. A.V. Nagasekhar, C.H. Cáceres, C. Kong, 3D characterization of intermetallics in a high pressure die cast Mg alloy using focused ion beam tomography. Mater. Charact. **61**, 1035–1042 (2010)
8. M. Yang, S.M. Xiong, Z. Guo, Characterisation of the 3-D dendrite morphology of magnesium alloys using synchrotron X-ray tomography and 3-D phase-field modelling. Acta Mater. **92**, 8–17 (2015)
9. A.K. Dahle, Y.C. Lee, M.D. Nave, P.L. Schaffer, D.H. StJohn, Development of the as-cast microstructure in magnesium-aluminium alloys. J. Light Met. **1**, 61–72 (2001)
10. L. Lu, A.K. Dahle, D.H. StJohn, Heterogeneous nucleation of Mg-Al alloys. Scripta Mater. **54**, 2197–2201 (2006)
11. Y. Wang, M. Xia, Z. Fan, X. Zhou, G.E. Thompson, The effect of Al$_8$Mn$_5$ intermetallic particles on grain size of as-cast Mg-Al-Zn AZ91D alloy. Intermetallics **18**, 1683–1689 (2010)
12. C. Simensen, N. Hansen, The effect of silicon upon alloys of Mg-2. 2 wt%Al-Mn. Z. Metallkd. **79**, 541–543 (1988)
13. B.C. Oberlander, C.J. Simensen, J. Svalestuen, A. Thorvaldsen, Phase diagram of liquid magnesium–aluminium–manganese alloys, in *Magnesium Technology* (1986), pp. 133–137

14. C.J. Simensen, B.C. Oberlander, J. Svalestuen, A. Thorvaldsen, Phase diagram for magnesium-aluminium-manganese above 650 °C. Z. Metallkd. **79**, 696–699 (1988)

15. C.J. Simensen, B.C. Oberlander, J. Svalestuen, A. Thorvaldsen, The Effect of Iron on Mg-4 wt.% Al-Mn Alloys. Z. Metallkd. **80**, 101–103 (1989)

16. G. Han, X. Liu, Phase control and formation mechanism of Al–Mn (–Fe) intermetallic particles in Mg–Al-based alloys with FeCl3 addition or melt superheating. Acta Mater. **114**, 54–66 (2016)

17. F. Pan, Z. Feng, X. Zhang, A. Tang, The types and distribution characterization of Al-Mn phases in the AZ61 magnesium alloy. Procedia Eng. **27**, 833–839 (2012)

18. B. Sundman, B. Jansson, J.-O. Andersson, The thermo-calc databank system. Calphad **9**, 153–190 (1985)

19. Y.W. Riddle, M.M. Makhlouf, Characterizing solidification by non-equilibrium thermal analysis, in *Magnesium Technology* (2003), pp. 101–106

20. R.H. Mathiesen, L. Arnberg, X-ray radiography observations of columnar dendritic growth and constitutional undercooling in an Al-30 wt%Cu alloy. Acta Mater. **53**, 947–956 (2005)

21. W.U. Mirihanage, K.V. Falch, I. Snigireva, A. Snigirev, Y.J. Li, L. Arnberg, R.H. Mathiesen, Retrieval of three-dimensional spatial information from fast in situ two-dimensional synchrotron radiography of solidification microstructure evolution. Acta Mater. **81**, 241–247 (2014)

22. L. Arnberg, R.H. Mathiesen, The real-time, high-resolution X-ray video microscopy of solidification in aluminum alloys. JOM **59**, 20–26 (2007)

23. T. Nagira, C.M. Gourlay, A. Sugiyama, M. Uesugi, Y. Kanzawa, M. Yoshiya, K. Uesugi, K. Umetani, H. Yasuda, Direct observation of deformation in semi-solid carbon steel. Scripta Mater. **64**, 1129–1132 (2011)

24. A.B. Phillion, R.W. Hamilton, D. Fuloria, A.C.L. Leung, P. Rockett, T. Connolley, P.D. Lee, In situ X-ray observation of semi-solid deformation and failure in Al-Cu alloys. Acta Mater. **59**, 1436–1444 (2011)

25. G. Reinhart, N. Mangelinck-Noël, H. Nguyen-Thi, T. Schenk, J. Gastaldi, B. Billia, P. Pino, J. Härtwig, J. Baruchel, Investigation of columnar-equiaxed transition and equiaxed growth of aluminium based alloys by X-ray radiography. Mater. Sci. Eng. A **413–414**, 384–388 (2005)

26. H. Yasuda, I. Ohnaka, K. Kawasaki, A. Sugiyama, T. Ohmichi, J. Iwane, K. Umetani, Direct observation of stray crystal formation in unidirectional solidification of Sn-Bi alloy by X-ray imaging. J. Cryst. Growth **262**, 645–652 (2004)

27. C.M. Gourlay, K. Nogita, A.K. Dahle, Y. Yamamoto, K. Uesugi, T. Nagira, M. Yoshiya, H. Yasuda, In situ investigation of unidirectional solidification in Sn-0.7Cu and Sn-0.7Cu-0.06Ni. Acta Mater. **59**, 4043–4054 (2011)

28. G. Zeng, S.D. McDonald, C.M. Gourlay, K. Uesugi, Y. Terada, H. Yasuda, K. Nogita, Solidification of Sn-0.7Cu-0.15Zn solder: in situ observation. Metall. Mater. Trans. A **45**, 918–926 (2014)

29. H. Yasuda, T. Nagira, M. Yoshiya, N. Nakatsuka, A. Sugiyama, K. Uesugi, K. Umetani, Development of X-ray Imaging for Observing Solidification of Carbon Steels. ISIJ Int. **51**, 402–408 (2011)

30. S. Shuai, E. Guo, A.B. Phillion, M.D. Callaghan, T. Jing, P.D. Lee, Fast synchrotron X-ray tomographic quantification of dendrite evolution during the solidification of MgSn alloys. Acta Mater. **118**, 260–269 (2016)

31. D. Casari, W.U. Mirihanage, K.V. Falch, I.G. Ringdalen, J. Friis, R. Schmid-Fetzer, D. Zhao, Y. Li, W.H. Sillekens, R.H. Mathiesen, α-Mg primary phase formation and dendritic morphology transition in solidification of a Mg-Nd-Gd-Zn-Zr casting alloy. Acta Mater. **116**, 177–187 (2016)

32. N. Otsu, A threshold selection method from gray-level histograms. Automatica **11**, 23–27 (1975)